

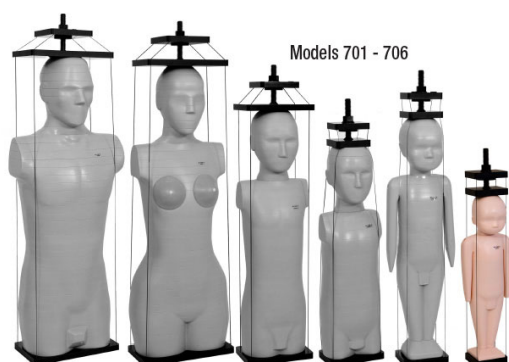
# A 2D driven 3D vessel segmentation algorithm for 3D digital subtraction angiography data

To cite this article: M Spiegel *et al* 2011 *Phys. Med. Biol.* **56** 6401

View the [article online](#) for updates and enhancements.

## Related content

- [Summation of DSA series](#)  
D Schuldhaus, M Spiegel, T Redel *et al.*
- [An automated method for accurate vessel segmentation](#)  
Xin Yang, Chaoyue Liu, Hung Le Minh *et al.*
- [Quantitative evaluation of noise reduction and vesselness filters for liver vessel segmentation on abdominal CTA images](#)  
Ha Manh Luu, Camiel Klink, Adriaan Moelker *et al.*



## Increase **Patient Safety** and Improve **Image Quality**

CIRS ATOM® phantoms are a full line of anthropomorphic, cross sectional dosimetry designed to investigate organ dose, whole body effective dose and delivery of therapeutic radiation doses. ATOM phantoms offer a number of advantages over other anthropomorphic dosimetry phantoms, including the wide range of ages and configurations. Phantoms can be sliced and drilled in a grid pattern for maximum flexibility of detector placement, or in an organ dosimetry pattern, which enables dose measurements to 22 radiosensitive organs using the fewest possible detectors. All phantoms include a custom fitted carry case.

**ATOM**  
DOSIMETRY PHANTOMS

Visit us at **ESTRO 2018**

**CIRS**

## A 2D driven 3D vessel segmentation algorithm for 3D digital subtraction angiography data

M Spiegel<sup>1,2,3,4</sup>, T Redel<sup>3</sup>, T Struffert<sup>2</sup>, J Hornegger<sup>1,4</sup> and A Doerfler<sup>2</sup>

<sup>1</sup> Pattern Recognition Lab, University Erlangen-Nuremberg, Erlangen, Germany

<sup>2</sup> Department of Neuroradiology, University Erlangen-Nuremberg, Erlangen, Germany

<sup>3</sup> Siemens AG Healthcare Sector, Forchheim, Germany

<sup>4</sup> Erlangen Graduate School in Advanced Optical Technologies (SAOT), Erlangen, Germany

E-mail: [martin.spiegel@informatik.uni-erlangen.de](mailto:martin.spiegel@informatik.uni-erlangen.de)

Received 9 June 2011, in final form 15 August 2011

Published 9 September 2011

Online at [stacks.iop.org/PMB/56/6401](http://stacks.iop.org/PMB/56/6401)

### Abstract

Cerebrovascular disease is among the leading causes of death in western industrial nations. 3D rotational angiography delivers indispensable information on vessel morphology and pathology. Physicians make use of this to analyze vessel geometry in detail, i.e. vessel diameters, location and size of aneurysms, to come up with a clinical decision. 3D segmentation is a crucial step in this pipeline. Although a lot of different methods are available nowadays, all of them lack a method to validate the results for the individual patient. Therefore, we propose a novel 2D digital subtraction angiography (DSA)-driven 3D vessel segmentation and validation framework. 2D DSA projections are clinically considered as gold standard when it comes to measurements of vessel diameter or the neck size of aneurysms. An ellipsoid vessel model is applied to deliver the initial 3D segmentation. To assess the accuracy of the 3D vessel segmentation, its forward projections are iteratively overlaid with the corresponding 2D DSA projections. Local vessel discrepancies are modeled by a global 2D/3D optimization function to adjust the 3D vessel segmentation toward the 2D vessel contours. Our framework has been evaluated on phantom data as well as on ten patient datasets. Three 2D DSA projections from varying viewing angles have been used for each dataset. The novel 2D driven 3D vessel segmentation approach shows superior results against state-of-the-art segmentations like region growing, i.e. an improvement of 7.2% points in precision and 5.8% points for the Dice coefficient. This method opens up future clinical applications requiring the greatest vessel accuracy, e.g. computational fluid dynamic modeling.

(Some figures in this article are in colour only in the electronic version)

## 1. Introduction

In modern neuroradiology, 3D rotational angiography (3D DSA) is an established and helpful technique to visualize complex cerebral vascular pathology and to guide interventional procedures. More and more 3D DSA data are also used for further quantitative analysis to support treatment planning and therapeutic procedures in patients with cerebrovascular diseases, e.g. aneurysms or stenosis (Heran *et al* 2006). This analysis requires reliable 3D vessel segmentation methods that delineate the boundary of the vessel as accurately as possible to come up with exact vessel measurements, e.g. vessel diameter, bifurcation angle of vessel branches, aneurysm dome sizes, etc. Since recent investigational techniques like hemodynamic simulations based on computational fluid dynamics (CFD) have become more and more popular within the research community of neuroradiology (Ford *et al* 2008, Castro *et al* 2006, Cebal *et al* 2005, Jou *et al* 2008, Spiegel *et al* 2011), the segmentation result and its corresponding mesh representation are the basis for even more reliable analysis. Small changes within the segmentation result may induce completely different flow patterns or wall shear stress distributions.

Hence, vessel segmentation results become more important for post-processing applications within the clinical environment. Accurate vessel segmentation based on 3D angiograms is challenging as it depends on the quality of the 3D DSA image that might vary for the individual patient. In clinical practice, there are a lot of factors that contribute to optimal and reproducible image quality. This includes the amount of injected contrast agent, the timing of injection, hemodynamic mixture of contrast agent and factors like blood flow cardiac output. Also reconstruction parameters may be different between patients (Strobel *et al* 2009, Zellerhoff *et al* 2005). Figure 1 gives examples of the influence of the different acquisition parameters on the final 3D DSA reconstructed images. The edge ramp between background and vessel intensities differs depending on the applied reconstruction kernel (see figure 1, upper part), e.g. some kernels yield an edge ramp whose slope is much higher than those generated by another kernel (Buzug 2008, Kak and Slaney 1988). These profiles provide an opening for different segmentation methods to differently interpret these edge ramps which may lead to varying vessel boundary positions. The ramp itself is also an indicator how the contrast agent is distributed at this position. In the case of sub-optimal injection timing, the contrast agent may leach out which leads to locally blurred vessel boundaries (see figure 1, lower part). Even if all acquisition parameters would be exactly the same, the final 3D DSA image volume will slightly differ because of the heterogeneous hemodynamic mixture of the contrast agent with the blood. Due to this, the validation of 3D DSA vessel segmentation results turns out to be rather difficult and thus 2D DSA imaging is still considered as the gold standard in quantitative evaluation and measurements (Peker *et al* 2009) being available during and after interventional evaluations. It is a challenge to validate any kind of segmentation methods so far and is especially true for the individual patient, while phantom models can be used for validation tests.

To overcome these challenges, a novel 3D vessel segmentation method is proposed in this paper that is driven by additional 2D vessel information. 2D DSA acquisitions are used as the validation base for 3D segmentations as well as a driving force to adapt an initial 3D segmentation. Each 3D DSA dataset comes automatically with 133 2D DSA projections showing the patient from various viewing angles. Moreover, these projections are registered and calibrated with the 3D DSA dataset. Selected 2D DSA images exhibit the advantage that the vessel boundaries are clearly visible and not blurred as it often happens in 3D DSA images. The novelty of our approach comprises an automatic segmentation algorithm formalizing a new global 2D/3D optimization function that smoothly combines 2D vessel information with

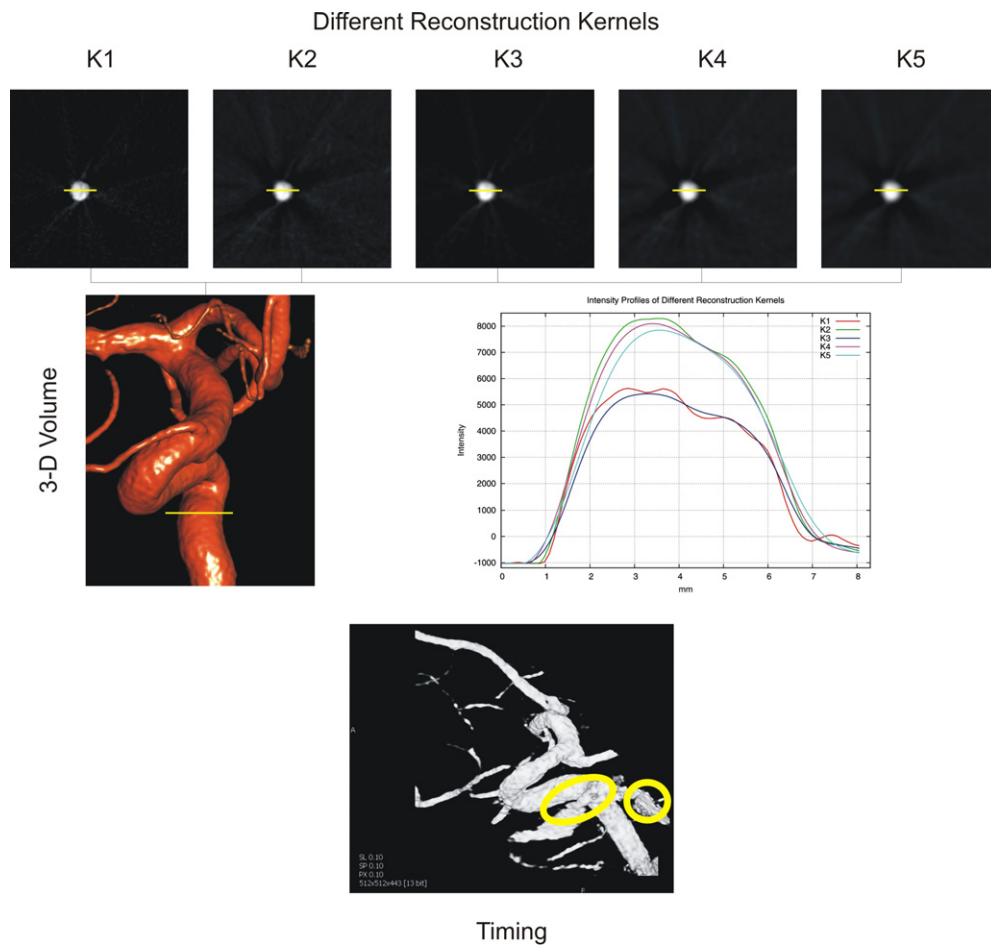


**Figure 1.** Influence parameters during the generation of a 3D DSA image: the upper part of the image shows the result using five different reconstruction kernels according with the intensity profiles. The lower part illustrates improper timing of contrast agent injection where veins are already visible (see the yellow circles).

an ellipsoid-based 3D vessel segmentation. Given a certain number of 2D DSA acquisitions, a forward projection of the current 3D segmentation is computed to be overlaid with the 2D acquisitions. The match between the forward projection and 2D DSA vessel information is used to drive and adapt the 3D vessel segmentation toward the 2D information. The entire workflow of our algorithm is depicted as a flow chart in figure 2(a). The remainder of this paper is organized as follows: (1) a brief overview is given on state-of-the-art vessel segmentation techniques, especially working with 3D DSA image data. (2) The applied 3D segmentation method is shortly illustrated delivering the initial segmentation result. (3) The adaptation process of the 3D vessel segmentation according to 2D DSA images will be introduced in detail which denotes the core part of this work. Section 4 delivers a quantitative insight on the applicability of this method.

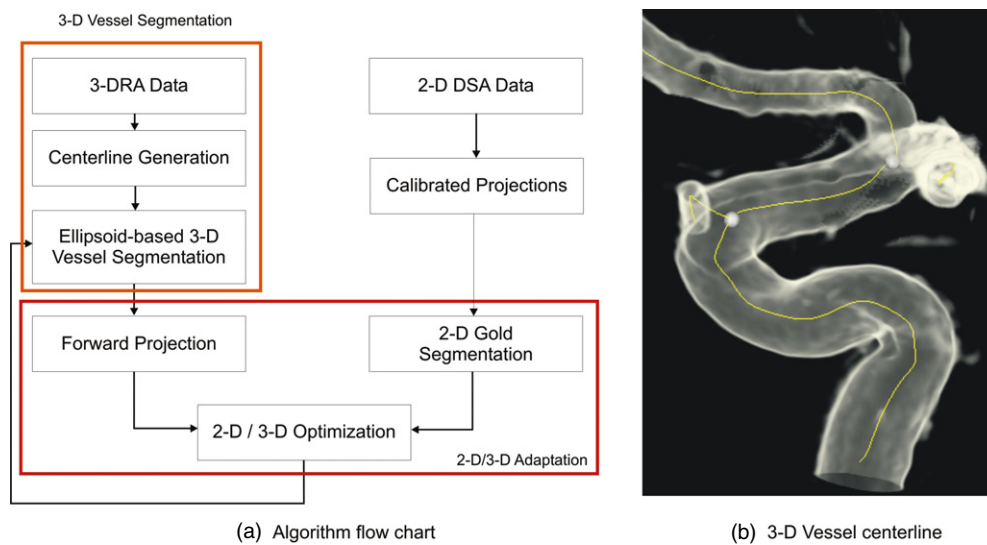


**Figure 2.** (a) An overview of the individual modules of the proposed 2D driven 3D vessel segmentation system. The orange box indicates the 3D vessel segmentation approach and the red box illustrates the components of the 2D/3D adaptation method. (b) A 3D vessel centerline (yellow line) is depicted which is used as the initialization for the 3D ellipsoid-based vessel segmentation. The spheres, illustrated in silver, represent bifurcation positions within the vessel centerline tree.

## 2. Related work

Within the last 10 years, a large variety of vessel detection, extraction and segmentation algorithms have been introduced for all kinds of imaging modalities (CT, MRI, 3D DSA) and applications. An extensive overview of this field is given by Lesage *et al* (2009) as well as by Kirbas and Quek (2004). The focus in this section is on vessel segmentation approaches using 3D DSA image data.

The 3D vessel segmentation approach used in this work is related to tubular-preserving vessel models. Yim *et al* (2001) employ a tubular deformable model in order to reconstruct vessel surfaces from 3D angiographic images. Another idea, proposed by Tyrrell *et al* (2007), models complex vessel trees by cylindrical super ellipsoids together with a joint estimation of vessel boundary and centerlines. This approach does not take explicit edge information into account for the vessel boundary detection. Wong and Chung (2007) introduced a probabilistic vessel axis tracing method for 3D angiograms to delineate the vessel boundary on cross sections. In a second step, the 3D vessel surface is defined by the minimum cost path on a weighted acyclic graph. Chang *et al* (2009) applied a region-growing segmentation approach on 3D DSA image data with a 3D extension for a deformable contour based on the charged fluid model. 4D minimal paths are used by Li and Yezzi (2007) to exploit and reconstruct 3D tubular structures on MR angiography and CT images. A non-parametric deformable model with high-order multiscale features is proposed by Hernandez and Frangi (2007) to segment vascular structures in 3D DSA and CT data. Gan *et al* (2005) applied a statistical vessel segmentation approach for 3D DSA images using expectation-maximization (EM) algorithm to estimate the intensity distribution of vessels based on maximum intensity projection (MIP)

images. Kang *et al* (2009) introduced a complementary geodesic distance field in order to smoothly register a given centerline onto the vessel lumen and to adapt an active tube model.

Another common approach is to apply multiscale filtering methods for determining vessel boundaries and to subsequently extract the vessel geometry from the image volume. Law and Chung (2007) introduced a combination of translated and rotated first derivative Gaussian filters to detect the intensity drop along vessels and aneurysms. The detection response is used to guide a level set segmentation framework. Tek *et al* (2005) described an algorithm for multiscale vessel detection and segmentation by using mean-shift analysis.

The literature contains some work which combines the 2D DSA image with different 3D imaging modalities, e.g. 3D DSA, CT or MR (Hipwell *et al* 2003, Chan *et al* 2004). Groher *et al* (2007) proposed a 2D–3D registration approach of abdominal angiographic data to register a catheter. Hentschke and Toennies (2009, 2010) registered a 2D DSA image with 3D DRA datasets to compare and validate flow simulation with the flow information encoded in 2D DSA images.

Although there are already ambitions to incorporate 2D information into 3D image datasets for various purposes, so far there is no 2D driven 3D vessel segmentation framework which adapts 3D vessel morphology by using 2D DSA information.

### 3. Methods

This section describes the proposed 2D driven 3D vessel segmentation approach. First, a short overview is given on the applied ellipsoid-based 3D vessel segmentation (Tyrrell *et al* 2007) which is enhanced by a local foreground/background intensity estimation using *Gaussian mixture models* (GMM) (Huang and Chau 2008). The methodology combining 2D and 3D vessel information will be discussed in detail.

#### 3.1. 3D vessel segmentation approach

The main purpose of our 3D segmentation approach is to detect and segment medium and large vessels within 3D DSA datasets delivering the input for the subsequent adaptation with 2D information.

*3.1.1. Prior knowledge, centerline and initialization.* 3D DSA is based on the direct intra-arterial injection of contrast agent. Due to the high contrast and the subtraction, it can be assumed *a priori* that the vessels appear in the highest intensity bins of the histogram. Thus, 3D DSA datasets consist of three different types of intensity classes, i.e. foreground (vessels), artifacts and background. The separation of these classes can be modeled by GMMs (Huang and Chau 2008) on a local or global level. This knowledge is utilized to design the *external energy* term of our 3D segmentation algorithm introduced later in this paper.

The vessels of a 3D DSA dataset enter the image volume from the bottom because of the *a priori* known acquisition setup, the anatomy of the cerebral vessel tree and the position of the patient on the table of a C-Arm system. Thus, the flow direction of the contrast agent is from bottom to top. This knowledge is used to automatically find the position of the largest vessel entering the volume. The Hough transformation (Jaehne 2011) for circles is applied on the most bottom slice of a 3D DSA image to localize the entering vessel associated with the largest diameter. This position is then taken as the seed point for the centerline computation method introduced by Guelsuen and Tek (2008). Figure 2(b) gives an example of the vessel centerline result. This seed point initialization is limited up to the selected volume of interest (VOI) used for secondary reconstruction. It may happen that this VOI was defined in a

way such that the major vessels enter laterally. In this case, the seed point has to be set manually. After centerline computation, each vessel branch is associated with one centerline that is represented as a  $B$ -spline. All centerline sections are stored within a tree structure, i.e. the centerline of the vessel lumen entering the volume is taken as the root within the tree structure. This structure easily reveals the father–son relationship between different vessel branches. The vessel centerline tree is used as an initialization for the ellipsoid-based vessel segmentation.

**3.1.2. Ellipsoid-based vessel segmentation.** Superellipsoids, ellipsoids or spheres are geometric primitives that are well suited for describing local vessel segments because such primitives being interleaved are able to approximate the tubular vessel structures in a smooth manner as mentioned in Tyrrell *et al* (2007). A unit sphere located within the coordinate center is implicitly defined as follows:

$$f(\mathbf{x}) = x_0^2 + x_1^2 + x_2^2 = 1, \quad (1)$$

where  $\mathbf{x} \in \mathbb{R}^3$  denotes a point on the surface of the sphere. To approximate localized vessel segments, a coordinate transformation has to be applied to allow arbitrary rotation, scale and translation, i.e. nine transformation parameters have to be estimated (three rotation, three scaling, three translation). The entire transformation function is expressed by

$$T(\mathbf{m}, \mathbf{x}) = \mathbf{R}(\mathbf{r})\mathbf{S}(\mathbf{s})\mathbf{x} + \mathbf{t}. \quad (2)$$

$\mathbf{R}$  represents the  $3 \times 3$  rotation matrix with the argument  $\mathbf{r} \in \mathbb{R}^3$  as rotation parameters. The scaling parameters  $\mathbf{s} \in \mathbb{R}^3$  are encoded within the  $3 \times 3$  diagonal matrix  $\mathbf{S}(\mathbf{s})$  and  $\mathbf{t} \in \mathbb{R}^3$  denotes the translation vector. All transformation parameters are summarized within the vector  $\mathbf{m} = (\mathbf{r}, \mathbf{s}, \mathbf{t}) \in \mathbb{R}^9$ . Thus, the implicit shape model can be rewritten as

$$f_T(\mathbf{m}, \mathbf{x}) := f(T(\mathbf{m}, \mathbf{x})) = f(\mathbf{R}(\mathbf{r})\mathbf{S}(\mathbf{s})\mathbf{x} + \mathbf{t}) \quad (3)$$

which separates the space into three different regions:

$$f_T(\mathbf{m}, \mathbf{x}) \in \begin{cases} < 1, & \text{if } \mathbf{x} \in \mathcal{I}(\mathbf{m}) \\ 1, & \text{if } \mathbf{x} \in \mathcal{S}(\mathbf{m}) \\ > 1, & \text{if } \mathbf{x} \in \mathcal{O} \setminus (\mathcal{I}(\mathbf{m}) \cup \mathcal{S}(\mathbf{m})), \end{cases} \quad (4)$$

where  $\mathcal{S}(\mathbf{m})$  and  $\mathcal{I}(\mathbf{m})$  denote the surface and the interior of an ellipsoid, respectively, and  $\mathcal{O}$  describes the image domain. This distinction will be later used as the *external energy* term within the global objective function to estimate the parameters properly. The previously computed centerlines are used to initialize the parameters, i.e. the center of the ellipsoids is placed on the centerlines. They are rotated such that the tangent vector of the centerline coincides with the local  $z$ -axis of the internal coordinate system of the ellipsoid. The curvature of the centerline is utilized to determine the number of ellipsoids that are required to approximate the vessel branch. In centerline sections with high curvature, the number of ellipsoids is increased while the ellipsoid scale in the  $z$ -direction is concurrently decreased. Areas of low curvature are treated vice versa. The ellipsoid scales pointing perpendicular to the vessel direction are initialized using cross-sectional radius intensity profiling. The parameter vector  $\mathbf{k} = (\mathbf{m}_0, \mathbf{m}_1, \dots, \mathbf{m}_{M-1}) \in \mathbb{R}^{9 \times M}$  holds all ellipsoid parameter of the entire model and  $M$  denotes the total number of ellipsoids used. For each ellipsoid, a specific local intensity threshold is estimated using GMM dividing the local image domain into foreground and background intensities. The threshold values are stored within the vector  $\mathbf{h} = (h_0, h_1, \dots, h_{M-1})^T \in \mathbb{R}^M$ . This estimate is further described later within this text when it comes to the definition of the *external energy* functional.



The initialized ellipsoid tube model is now optimized such that the model evolves toward the boundary of the vessels according to a predefined energy. The total energy functional,  $G_{\text{tot}}(\mathbf{k}, \mathbf{h})$ , is composed of two terms:

$$G_{\text{tot}}(\mathbf{k}, \mathbf{h}) : \mathbb{R}^{9 \times M} \times \mathbb{R}^M \rightarrow \mathbb{R}$$

$$\arg \min_{\mathbf{k}, \mathbf{h}} G_{\text{tot}}(\mathbf{k}, \mathbf{h}) = \alpha G_{\text{ext}}(\mathbf{k}, \mathbf{h}) + (1 - \alpha) G_{\text{int}}(\mathbf{k}), \quad (5)$$

where  $G_{\text{ext}}(\mathbf{k}, \mathbf{h})$  and  $G_{\text{int}}(\mathbf{k})$  denote the external and *internal energy* term, respectively, and  $\alpha$  defines the weighting factor.

The *internal energy* term is associated with the inherent characteristics of the tube model, i.e. the pose parameters between two subsequent ellipsoids have to be modeled in a smooth way. For that purpose, the *internal energy* term consists of three cubic *B-splines* (Klein *et al* 1997, Tauber *et al* 2009) ( $\{B_i\}_{i=0}^2$ ) to ensure smoothness in terms of rotation, scaling and translation between neighboring ellipsoids:

$$G_{\text{int}}(\mathbf{k}) = \sum_{i=0}^2 \int_{L_i} |B_i(l, \mathbf{k})'| dl + \int_{L_i} |B_i(l, \mathbf{k})''| dl, \quad (6)$$

where  $B_i(l, \mathbf{k})'$  and  $B_i(l, \mathbf{k})''$  represent the first and second derivative of the *B-spline*  $B_i$  with respect to the parameters  $\mathbf{k}$ .  $L_i$  is the total length of the *B-spline* and  $l$  is the position on the spline. The first *B-spline*,  $B_0(l, \mathbf{k})$ , is a *B-spline* in 2D and it describes the change of orientation between two ellipsoids. Its sample points  $\mathbf{q}_r = (l, \phi) \in \mathbb{R}^2$  are defined by  $l$  and  $\phi$  denoting the length position of the ellipsoid center on the *B-spline* and the change of the orientation angle between two ellipsoids, respectively.  $B_1(l, \mathbf{k})$  is a *B-spline* in 3D covering the change of scales between subsequent ellipsoids. The sample points are defined as  $\mathbf{q}_s = (l, s_0, s_1) \in \mathbb{R}^3$  where  $s_0$  and  $s_1$  represent the scaling in the x-y directions of the ellipsoid. The last *B-spline*,  $B_2(l, \mathbf{k})$ , represents the centerline in 3D which is now defined by the center points of the ellipsoids  $\mathbf{q}_t = (t_0, t_1, t_2) \in \mathbb{R}^3$ . Equation (6) regularizes the changes of the ellipsoid parameters  $\mathbf{k}$  induced by the *external energy* such that the entire ellipsoid model represents the vessel tree in a smooth manner.

The *external energy* term is responsible to drive the model toward the surrounding vessel structures. A 3D DSA image consists of foreground and background voxel intensities as already mentioned in section 3.1.1. Given this prior knowledge, our ellipsoid vessel shape model tries to separate the image domain into these two regions as good as possible. This is evaluated by counting the number of foreground and background voxel intensities within the sets  $\mathcal{S}(\mathbf{k}_i)$  and  $\mathcal{I}(\mathbf{k}_i)$ . Depending on the local intensity threshold  $h_i$  and the ellipsoid parameters  $\mathbf{k}_i$ ,  $\mathcal{F}(\mathbf{k}_i, h_i) \subset (\mathcal{S}(\mathbf{k}_i) \cup \mathcal{I}(\mathbf{k}_i))$  defines the set of foreground voxels. Consequently,  $\mathcal{B}(\mathbf{k}_i, h_i) \subset (\mathcal{O} \setminus \mathcal{F}(\mathbf{k}_i, h_i))$  describes the set of background voxels which is constrained by the ellipsoid bounding box. The *external energy* is described as

$$G_{\text{ext}}(\mathbf{k}, \mathbf{h}) = \frac{1}{M} \sum_{i=0}^{M-1} \left( \frac{|\mathcal{F}(\mathbf{k}_i, h_i)| - |\mathcal{B}(\mathbf{k}_i, h_i)|}{|\mathcal{F}(\mathbf{k}_i, h_i) \cup \mathcal{B}(\mathbf{k}_i, h_i)|} \right)^{-1}. \quad (7)$$

The initialization of the ellipsoid pose parameters (described in the beginning of this section) and the estimation of the local intensity threshold  $h_i$  ensure that the number of foreground voxels  $|\mathcal{F}(\mathbf{k}_i, h_i)|$  is always greater than the number of background voxels  $|\mathcal{B}(\mathbf{k}_i, h_i)|$ . The GMM modeling is used to estimate the local intensity threshold within a box which is centered at the current ellipsoid center and its size ranges between  $32 \times 32 \times 32$  and  $64 \times 64 \times 64$  depending on the current vessel scales. The goal is to minimize equation (7) such that the pose parameters of the ellipsoids perfectly match to the local vessel structures. Hence, the ideal situation



would be if  $|\mathcal{B}(\mathbf{k}_i, h_i)|$  becomes zero, i.e. the fraction in equation (7) would be 1. In real datasets, however,  $|\mathcal{B}(\mathbf{k}_i, h_i)|$  is greater than zero making the fraction smaller than 1 such that the reciprocal delivers a final value which is greater than 1. Thus, the *external energy* term becomes minimal if the parameters  $\mathbf{k}$  are estimated such that  $|\mathcal{F}(\mathbf{k}_i, h_i)|$  is maximized while  $|\mathcal{B}(\mathbf{k}_i, h_i)|$  becomes very small given a certain threshold  $h_i$ . This local foreground/background estimation ensures that the *external energy* adapts to vessel structures exhibiting even a high intensity variation throughout the entire dataset.

The optimal ellipsoid parameters are found by minimizing the total energy functional  $G_{\text{tot}}(\mathbf{k}, \mathbf{h})$  together with the local intensity thresholds. Since our model is initialized by a pre-computed centerline and cross-sectional radius profile estimation, the initial parameter set is located near the global optimum. Hence, gradient descent is applied to optimize our energy functional using finite differences.

### 3.2. 2D driven 3D adaptation

The methods described in section 3.1.2 deliver a parametric 3D vessel segmentation result that is purely driven by 3D image data. As already mentioned within the introduction, the appearance of the 3D DSA volume data depends on four influence factors, i.e. amount of contrast agent, time of injection, hemodynamic mixture of the contrast agent and the applied reconstruction kernel. Therefore, a comparison of the 3D segmentation result with 2D DSA segmentation is necessary. 2D DSA projections are manually selected to validate the 3D segmentation result via overlay matching. The mapping of the volumetric data onto the 2D DSA images is known by calibration (Hoppe et al 2007). This comparison is performed by forward projection of the 3D vessel segmentation using ray casting (Sherouse et al 1990). The local discrepancies between the 2D vessel information and the forward projection is now formalized within a new objective function which utilizes the 3D parametric segmentation. This leads to a new 2D/3D *external energy* functional  $G_{\text{ext}2\text{D}/3\text{D}}(\mathbf{k})$  measuring the differences between 2D and 3D segmentations. It is defined as follows:

$$G_{\text{ext}2\text{D}/3\text{D}}(\mathbf{k}) = \sum_{i=0}^{Q-1} \sum_{\mathbf{u}} (w(i, \mathbf{u}) - v(i, \mathbf{u}, \mathbf{k}))^2 \quad (8)$$

where  $Q$  indicates the number of projection images used to adapt the 3D segmentation result and  $w(i, \mathbf{u})$  denotes the intensity value of the 2D ground truth segmentation of the  $i$ th projection image at position  $\mathbf{u} = (x_1, x_2) \in \mathbb{R}^2$ . The intensity value of the forward projection  $v(i, \mathbf{u}, \mathbf{k})$  is given by the *maximum intensity projection* (MIP). The novel 2D/3D *external energy* functional forms a new total energy that is defined as follows:

$$G_{\text{tot}2\text{D}/3\text{D}}(\mathbf{k}) : \mathbb{R}^{9 \times M} \rightarrow \mathbb{R}$$

$$\arg \min_{\mathbf{k}} G_{\text{tot}2\text{D}/3\text{D}}(\mathbf{k}) = \alpha G_{\text{ext}2\text{D}/3\text{D}}(\mathbf{k}) + (1 - \alpha) G_{\text{int}}(\mathbf{k}). \quad (9)$$

The *external energy* term in equation (5) is replaced by the new 2D driven 3D external force  $G_{\text{ext}2\text{D}/3\text{D}}(\mathbf{k})$  while the *internal energy* is kept. The *internal energy* functional denotes an important regularization term during 2D/3D adaptation because the 3D information is lost while performing the forward projection. Thus, the *internal energy* ensures that the 3D ellipsoid model does not deform toward unrealistic vessel approximations or twisting.

As illustrated in equation (8), the *sum of squared differences* (SSD) between the 2D ground truth and the forward projection is applied as a similarity measure. Considering the 2D/3D medical image registration literature, however, there might be other similarity measures

(Penney *et al* 1998) like *normalized cross-correlation*, etc, which might lead to similar results.

#### 4. Evaluation and results

Our 2D driven 3D vessel segmentation method was evaluated on one phantom image and ten patient datasets with different cerebrovascular diseases. The datasets were acquired at the Department of Neuroradiology (University Erlangen-Nuremberg) during endovascular interventions using a flat-panel equipped C-Arm System (AXIOM Artis dBA, Siemens AG Healthcare Sector, Forchheim, Germany). The volume dimensions range between  $512 \times 512 \times 390$  and  $512 \times 512 \times 511$  with an isotropic voxel spacing of 0.1 mm. A 3D DSA image volume is commonly reconstructed given 133 2D DSA projections that were acquired while the C-Arm rotates around the patient's head. Three out of the 133 projections were selected showing the volume from different viewing angles to perform the 2D/3D match. The viewing angle difference of the selected projections varies from  $10^\circ$  to  $170^\circ$  which ensures an adaptation of the 3D segmentation according to sufficiently different 2D projections. The novel idea of using 2D DSA projection in order to refine the given 3D ellipsoid-based segmentation result is compared to the clinical established threshold-based region growing segmentation. Hence, three different 3D vessel segmentations were computed, i.e. region-growing, 3D ellipsoid and 2D driven 3D ellipsoid segmentation. The marching cubes algorithm (Lorensen *et al* 1987) was applied to visualize the 3D segmentation results as meshes.

##### 4.1. Methods of evaluation

Since the setup of 3D gold standard segmentations given 3D DSA data is rather difficult due to the dependency of many parameters (hemodynamic mixture of the contrast agent, applied reconstruction kernel, start and time of acquisition), we focus in this work on pure 2D related evaluation measures. The 3D segmentation result is being forward projected into 2D defining the vessels of interest within the used 2D DSA projections for adaptation (see figures 3 and 4, left column (DSA) with the red boxes). These vessels were manually outlined and approved by a neuroradiologist to be used as the gold standard segmentation in 2D. The overlap between the forward projection of a 3D segmentation result and the 2D gold standard was evaluated using two measurements:

Dice coefficient and precision. The Dice coefficient is defined by

$$\text{Dice} = \frac{2|X \cap Y|}{|X| + |Y|}, \quad (10)$$

where  $X$  denotes all pixels of the gold standard segmentation and  $Y$  all pixels of the forward projection.

The precision (P) is expressed by the following formula:

$$P = \frac{TP}{TP + FP}, \quad (11)$$

where TP is the number of true positives and FP the number of false positives. In our case, TP is given by the number of pixels that are consistently segmented as vessel both by the specific 3D segmentation method and within the gold standard. FP is the number of pixels that have been falsely classified as vessel structure. The Hausdorff distance is applied to measure and visualize the deformations before and after 2D driven 3D optimization. The evaluation regarding 2D measurements is four-sided.

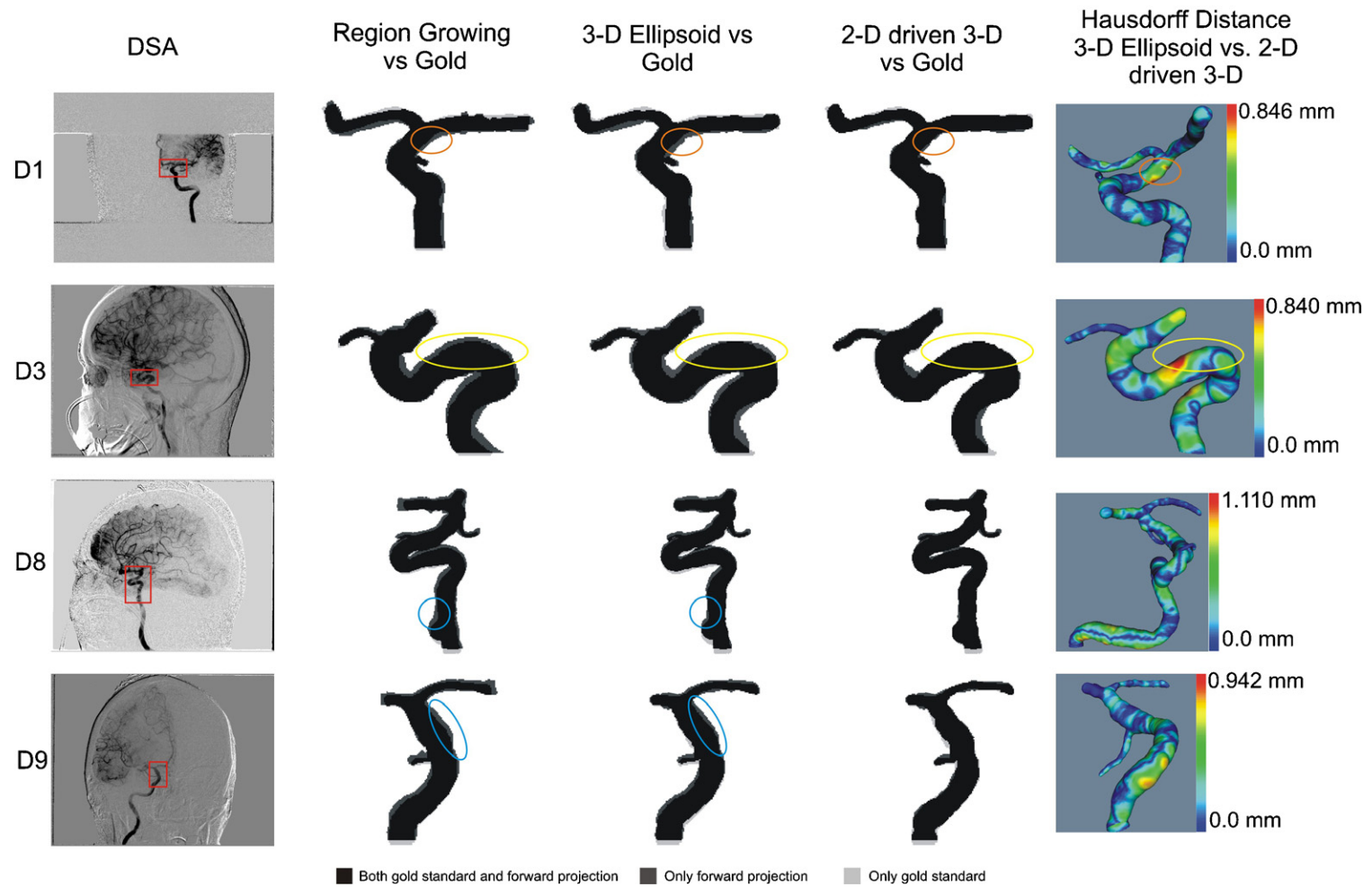


**Figure 3.** This set of images shows evaluation results concerning four datasets. In the left column, one of the three projection images is illustrated that was used to adapt the 3D ellipsoid segmentation. The three middle columns depict 2D comparison of the forward projections originating from three different vessel segmentation methods, i.e. region growing, 3D ellipsoid and 2D driven 3D segmentation. The rightmost column gives a 3D impression of the deviations. The meaning of the circles is described within section 4.

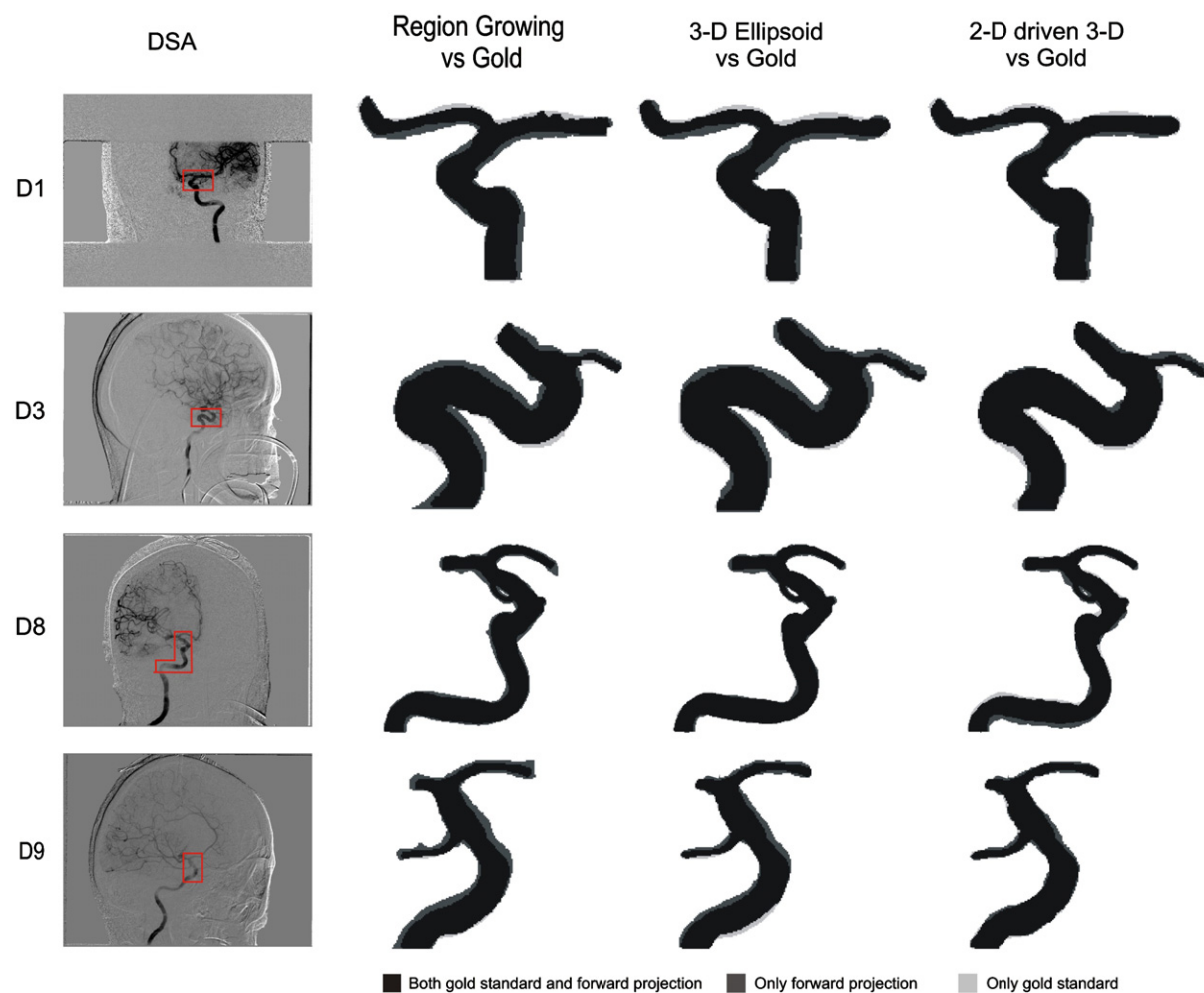


**Figure 4.** This set of images shows qualitative evaluation results concerning four datasets. The projections were not part of the optimization set in order to measure the overall fit of the 2D driven 3D segmentation approach. The three columns on the right depict 2D comparison of the forward projections originating from three different vessel segmentation methods, i.e. region growing, 3D ellipsoid and 2D driven 3D segmentation.

- (1) A simple intensity region growing segmentation is applied which was started by a manual seed point. The intensity range was chosen by a neuroradiologist based on his working experience with 3D DSA data. The forward projections are compared to the 2D gold standard segmentations.
- (2) The pure 3D driven ellipsoid-based segmentation result (see section 3.1.2) is being forward projected to measure the overlap with the 2D gold standard segmentation.
- (3) The forward projections of our novel 2D driven 3D segmentation approach are compared to 2D gold standard segmentations. This allows judging the overlap match before and after 2D/3D adaptation.
- (4) Another three 2D DSA projections are selected that were not part of the 2D/3D adaptation process. These three 2D DSA projections were again manually outlined. Then the 2D driven 3D segmentation result is forward projected against these three 2D projections and the overlap is measured. This measurement allows us to come up with a statement about the overall fit of the 2D adapted 3D segmentation result toward other 2D projections.

#### 4.2. Experimental results

This section describes the segmentation results concerning the three different segmentation approaches. All experiments were performed on a Intel Core2 CPU with 2 GHz, 4GB of main memory and NVIDIA Quadro FX 2500M graphics card. The algorithms were completely implemented in C++ whereas the computation of the forward projection was done using OpenGL. The overall intension of incorporating 2D information into the 3D segmentation process is to be able to come up with quantitative measurements in 3D that are taken on a valid base. Therefore, our experimental setup is split into two categories, i.e. phantom-based and patient-specific experiments.

**4.2.1. Phantom experiment.** Our vessel phantom (see figure 5) is made up of a plastic tube exhibiting an inner diameter of 3.6 mm and a wall thickness of 1.3 mm. The phantom experiment was conducted in order to set up an ideal acquisition environment. This environment eliminates some disturbing factors in contrast to a real patient acquisition, i.e. there is no patient movement, the plastic tube was completely filled with the contrast agent such that it is homogenously distributed without air blebs and the vessel diameter is known *a priori*. The phantom results are really promising. The quantitative results are illustrated in tables 1 and 2 (column P). Looking at table 1 summarizing the results concerning the optimization projections: the 2D driven 3D approach shows that an improvement of about 7% points against the 3D ellipsoid-based segmentation and almost 13% over the result computed by region growing. Also the results for those projections which were not used for optimization show a clear outperformance of our 2D driven 3D method over the other two methods (see table 2).

**4.2.2. Patient-specific experiments.** This section describes our experiments that were conducted with patient-specific data. An overview on the segmentation results is given in table 1. Figure 3 illustrates the qualitative results. Considering the quantitative results given in table 1, it turns out that the 2D driven 3D vessel segmentation approach outperforms the other two segmentation methods.

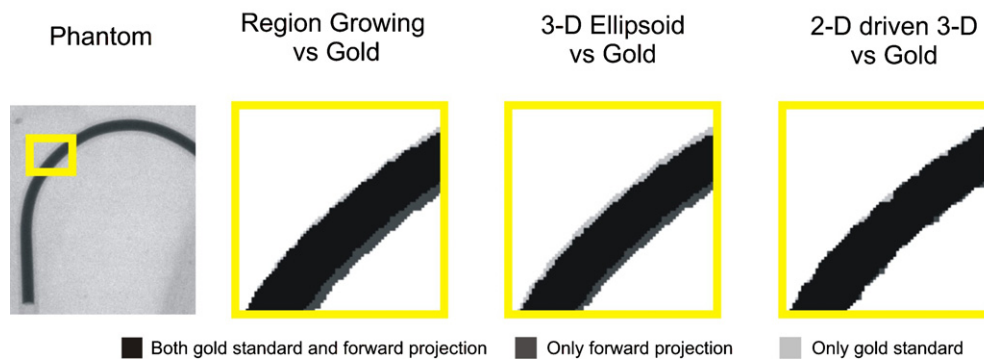


**Figure 5.** Qualitative results concerning the phantom experiments. The projections shown in this figure were part of the optimization set. The yellow boxes represent the zoomed region for illustration purposes.

Regarding the evaluation measurements within the optimization set (1), the region growing approach achieves an overall fit of 89.1% (Dice) and 83.2% (precision). The 3D ellipsoid segmentation shows a slightly better result, i.e. 89.4% (Dice) and 87.0% (precision). A major improvement, however, could be achieved by the 2D driven 3D segmentation approach, i.e. 95.2% (Dice) and 94.2% (precision).

Moreover, table 2 and figure 4 show that this novel 2D/3D segmentation method delivers better results than the other two techniques even for projections that have not been part of the optimization set. There, the average Dice coefficient and precision reveal 91.6% and 89.2%, respectively. The region growing and 3D ellipsoid-based segmentation end up on average with 90.0% and 90.9% for Dice—83.5% and 86.8% for precision, respectively.

Comparing the qualitative segmentation results of the region growing approach with the 3D ellipsoid method, the vessel diameters appear slightly thicker within the region growing results (see figure 3, blue circles). The 2D/3D adapted ellipsoid segmentation result is shown within the fourth column of figure 3. The new algorithm deforms smoothly toward the boundary of the given 2D gold standard segmentation. The deformations are depicted using the Hausdorff distance before and after 2D/3D optimization. The orange and yellow circles within figure 3 illustrate exemplarily the differences between the three segmentation results. The 2D driven 3D approach is able to fit to the gold standard segmentations in almost all regions. Those remaining regions that are not covered by the 2D/3D model originate due to external influence factors, e.g. vessel movement due to the beating heart or patient movement.

## 5. Discussion

When it comes to measurements of vessel diameters during treatment planning, 2D DSA projections denote the gold standard image modality to perform these measurements. Therefore, this 2D driven 3D vessel segmentation method can be considered as a general approach to validate 3D vessel segmentations based on 3D DSA image data. Independent of the applied segmentation algorithm, it is possible to judge the 3D segmentation result by means of forward projection and comparison with corresponding 2D DSA projections. The new *external energy* force introduced in section 3.2 can be applied as a regularizer for various 3D vessel segmentation methods based on different mathematical principles, e.g.

**Table 1.** Summary of the 2D/2D evaluation results. The numbers are average values given in % which measure the overlap (Dice, precision) between the forward projection of a 3D segmentation method and the corresponding ground truth vessel segmentation of the selected 2D DSA projection images. Here, the result against the incorporated 2D DSA projections is shown. P, D and Std. Dev. abbreviate phantom, dataset and standard deviation, respectively.

Method			Average 2D/2D measurements—part of the optimization set										Avg.	Std. Dev.
Dataset		P	D1	D2	D3	D4	D5	D6	D7	D8	D9	D10		
Dice	Region growing	86.1	91.4	91.4	89.7	90.1	90.4	88.6	85.8	88.6	85.8	89.2	<b>89.1</b>	2.0
	3D ellipsoid	91.4	89.8	92.9	90.4	89.7	91.8	87.0	86.0	89.8	88.5	88.4	<b>89.4</b>	2.1
	2D driven 3D	98.1	96.7	96.1	95.0	96.2	95.6	93.4	93.2	96.9	93.9	95.0	<b>95.2</b>	1.3
Precision	Region growing	76.3	87.1	86.2	84.9	86.1	84.7	82.4	77.9	83.3	78.0	81.4	<b>83.2</b>	3.3
	3D ellipsoid	85.8	91.9	91.1	85.0	85.1	90.5	84.2	83.9	88.4	85.4	84.6	<b>87.0</b>	3.1
	2D driven 3D	97.2	96.0	95.9	94.7	95.8	95.8	90.4	90.0	96.1	93.4	94.3	<b>94.2</b>	2.3



**Table 2.** Summary of the 2D/2D evaluation results. The numbers are average values given in % which measure the overlap (Dice, precision) between the forward projection of a 3D segmentation method and the corresponding ground truth vessel segmentation of the selected 2D DSA projection images. Here, three other 2D DSA projections were selected that are *not* part of the optimization set in order to measure the overall match of our 2D driven 3D method. P, D and Std. Dev. abbreviate phantom, dataset and standard deviation, respectively.

Method		Average 2D/2D measurements—not part of the optimization set											Avg.	Std. Dev.
Dataset	P	D1	D2	D3	D4	D5	D6	D7	D8	D9	D10			
Dice	Region growing	86.7	92.0	91.0	90.2	92.7	91.9	91.1	85.4	91.2	85.9	88.5	<b>90.0</b>	2.6
	3D ellipsoid	90.8	91.3	92.0	89.1	92.6	93.4	91.2	85.5	93.6	88.8	91.8	<b>90.9</b>	2.5
	2D driven 3D	95.0	93.4	92.0	91.0	92.8	92.4	91.9	89.6	89.8	92.6	90.2	<b>91.6</b>	1.3
Precision	Region growing	77.5	88.5	84.0	84.6	87.9	86.2	84.4	77.6	84.1	76.9	80.1	<b>83.5</b>	4.0
	3D ellipsoid	85.6	89.6	88.0	81.5	87.1	92.1	85.9	83.2	90.2	84.2	86.3	<b>86.8</b>	3.3
	2D driven 3D	93.1	92.9	89.2	87.1	91.5	92.2	87.9	85.9	87.1	89.8	87.9	<b>89.2</b>	2.4

other parametric segmentation algorithms, level sets or graph cuts. We applied the SSD as a cost function due to the fact that we dealt only with segmentations in 2D as well as in 3D. Within the evaluation, three 2D DSA projections were used to adapt the 3D segmentation but this approach is open to incorporate as many projections as the user wants to be used. Another approach would be not to manually segment the vessel of interest within the 2D DSA projections but to incorporate the projections as is. This would imply use of different cost functions for the 2D/3D external force, e.g. normalized cross-correlation, pattern intensity, gradient difference, etc. One might argue that the original 2D edge information can be already integrated within the reconstruction process by manual outlining of all 133 2D DSA projections used for reconstruction, and finally reconstructing a binary image volume. This, however, is not feasible within clinical routine because this manual outlining will take several hours. Our 2D driven 3D approach has been developed with respect to clinical workflows and aspects, i.e. during stent or coil planning, physicians choose selected 2D DSA projections to measure the vessel diameter or aneurysm neck size to decide which stent or coil type has to be used to get an optimal therapeutic outcome. Within our integrated 2D/3D segmentation framework, the adaptation of the 3D vessel segmentation to the chosen 2D projection can be easily done.

Moreover, this segmentation approach helps to reduce the influence of acquisition- and reconstruction-related factors as described in the introduction. Different reconstruction kernels (Buzug 2008, Kak and Slaney 1988) exhibit inherently different edge enhancement leading to varying edge ramps (see figure 1), i.e. the original edge information which is present within the 2D DSA projections (being used for reconstruction) has not been used so far to drive the segmentation algorithm toward the real vessel edge. With the incorporation of the 2D projections, however, this information is now used a second time (first for reconstruction and second for vessel segmentation) within our new 2D driven 3D ellipsoid segmentation approach to ensure that the vessel edges of the 3D fit to the edges given in 2D. The 2D data available are based either on dedicated 2D DSA acquisitions or on the 133 acquisition used for the 3D reconstruction, while both are different in dose and therefore in the inherent noise level that will become a next step for an automatic segmentation approach of the 2D data. Both cases are usable for our manual segmentation approach, proving the concept.

A 3D ellipsoid-based segmentation is used to approximate the vessel structures with a strong tubular regularizer. The advantages of this segmentation algorithm denote the ability to adapt to local vessel branches and its deviations by interleaving ellipsoids, as already mentioned in Tyrrell *et al* (2007). We enhanced this approach by using GMMs to perform local adaptive threshold estimation which ensures that local intensity variations within vessels are covered in a more accurate way. The results show (see table 3, rightmost column) that the 3D ellipsoid-based model outperforms the region growing approach.

While performing a forward projection onto the three selected 2D projections, the 3D information is lost. The deformations computed within 2D may cause changes within the 3D segmentation that may lead toward unrealistic vessel appearance. Now, the advantage of the parametric 3D vessel segmentation comes into play because those deviations can be easily avoided by the *internal energy* force introduced in section 3.1.2. This internal force watches the parameter changes of the interleaved ellipsoids concerning rotation, scaling and translation and penalizes those changes featuring highly non-tubular vessel structures.

The overall 2D driven 3D segmentation results look promising, even if there are still some remaining areas where our 2D/3D adaptation could not properly deform toward the 2D vessel boundaries. There are three reasons which might cause this behavior: (1) patient movement between the different 2D DSA projections may cause an area of conflict showing

an inconsistent vessel situation. (2) The 2D DSA projections were arbitrarily selected with the only condition that the vessel is depicted from different viewing angles. This may imply vessel movement between the projections due to different phases of the cardiac cycle. (3) The internal force keeps the model from deformation toward these areas because the gain of cost reduction concerning the external force is too little compared to the increase of the costs induced by the internal term.

## 6. Conclusion and outlook

The algorithm presented in this work illustrates the first attempt to incorporate 2D projection information into a 3D vessel segmentation method for 3D DSA data. Our results show that the match between the forward projection of 3D segmentation volume with manually outlined 2D DSA vessel segmentations is not identical as it is supposed to be for an ideal calibrated case. This occurs because of the influence factors that appear during 3D DSA acquisition. Our 2D driven 3D method opens up the possibility of driving the 3D vessel segmentation results toward previously selected 2D information. This step enables us to perform quantitative vessel measurements in 3D on a more valid base. This approach serves as a key module toward an automatic 2D/3D vessel segmentation framework. The next steps will be to extend this approach by a semi-automatic 2D vessel segmentation algorithm such that the 2D gold standard segmentations can be omitted (Schuldhuis *et al* 2011a, 2011b). This will boost the feasibility of this approach within a clinical environment.

## Acknowledgments

The authors gratefully acknowledge the funding of the Erlangen Graduate School in Advanced Optical Technologies (SAOT) by the German National Science Foundation (DFG) in the framework of the excellence initiative.

## References

- Buzug Thorsten M 2008 *Computed Tomography—From Photon Statistics to Modern Cone-Beam CT* (Berlin: Springer)
- Castro M A, Putman C M and Cebal J R 2006 Patient-specific computational fluid dynamics modeling of anterior communicating artery aneurysms a study of the sensitivity of intra-aneurysmal flow patterns to flow conditions in the carotid arteries *Am. J. Neuroradiol.* **27** 2061–8
- Cebal J R, Castro M A, Appanaboyina S, Putman C M, Millan D and Frangi A F 2005 Efficient pipeline for image-based patient-specific analysis of cerebral aneurysm hemodynamics: technique and sensitivity *IEEE Trans. Med. Imaging* **24** 457–67
- Chan H, Chung A, Yu S and Wells W 2004 2D–3D vascular registration between digital subtraction angiographic (DSA) and magnetic resonance angiographic (MRA) images *IEEE Int. Symp. on Biomedical Imaging: Nano to Macro* pp 708–11
- Chang H, Duckwiler G, Valentino D and Chu W 2009 Computer-assisted extraction of intracranial aneurysms on 3D rotational angiograms for computational fluid dynamics modeling *Med. Phys.* **36** 5612–21
- Ford M D, Lee S W, Lownie S P, Holdsworth D W and Steinman D A 2008 On the effect of parent-aneurysm angle on flow patterns in basilar tip aneurysms: towards a surrogate geometric marker of intra-aneurysmal hemodynamics *J. Biomech.* **41** 241–8
- Gan R, Wong W and Chung A 2005 Statistical cerebrovascular segmentation in three-dimensional rotational angiography based on maximum intensity projections *Med. Phys.* **32** 3017–28

- Groher M, Bender F, Hoffmann R-T and Navab N 2007 Segmentation-driven 2D–3D registration for abdominal catheter interventions *Medical Image Computing and Computer-Assisted Intervention* vol 4792 ed A Maeder, N Ayache and S Ourselin (Berlin: Springer) pp 527–35
- Guelsuen M and Tek H 2008 Robust vessel tree modeling *Medical Image Computing and Computer-Assisted Intervention* (Berlin: Springer) pp 603–11
- Hentschke C and Toennies K-D 2009 Intensity-based registration of 2D-DSA and 3D-DSA data sets for flow simulation in intracranial aneurysms *Proc. Vision, Modeling and Visualization (VMV) (Braunschweig)* pp 375–6
- Hentschke C and Toennies K-D 2010 Automatic 2D/3D-registration of cerebral DSA data sets *Bildverarbeitung für die Medizin (BVM2010)* (Aachen: Springer) pp 162–6
- Heran N S, Song J K, Namba K, Smith W, Niimi Y and Berenstein A 2006 The utility of DynaCT in neuroendovascular procedures. *Am. J. Neuroradiol.* **27** 330–2
- Hernandez M and Frangi A 2007 Non-parametric geodesic active regions: method and evaluation for cerebral aneurysms segmentation in 3DRA and CTA *Med. Image Anal.* **11** 224–41
- Hipwell J H, Penney G P, McLaughlin R A, Rhode K, Summers P, Cox T C, Byrne J V, Noble J A and Hawkes D J 2003 Intensity-based 2D–3D registration of cerebral angiograms *IEEE Trans. Med. Imaging* **22** 1417–26
- Hoppe S, Noo F, Dennerlein F, Lauritsch G and Hornegger J 2007 Geometric calibration of the circle-plus-arc trajectory *Phys. Med. Biol.* **52** 6943–60
- Huang Z-K and Chau K-W 2008 A new image thresholding method based on Gaussian mixture model *Appl. Math. Comput.* **205** 899–907
- Jaehne B 2011 *Digital Image Processing* (Berlin: Springer)
- Jou L, Lee D, Morsi H and Mawad M 2008 Wall shear stress on ruptured and unruptured intracranial aneurysms at the internal carotid artery *Am. J. Neuroradiol.* **29** 1761–7
- Kak A and Slaney M 1988 *Principles of Computerized Tomographic Imaging* (Piscataway, NJ: IEEE Press)
- Kang D G, Suh D C and Ra J B 2009 Three-dimensional blood vessel quantification via centerline deformation *IEEE Trans. Med. Imaging* **28** 405–14
- Kirbas C and Quek F 2004 A review of vessel extraction techniques and algorithms *ACM Comput. Surv.* **36** 81–121
- Klein A, Lee F and Amini A 1997 Quantitative coronary angiography with deformable spline models *IEEE Trans. Med. Imaging* **16** 468–82
- Law M and Chung A 2007 Vessel and intracranial aneurysm segmentation using multi-range filters and local variances *MICCAI' 07: Proc. 10th Int. Conf. on Medical Image Computing and Computer-Assisted Intervention* (Berlin: Springer) pp 866–74
- Lesage D, Angelini E, Bloch I and Funka-Lea G 2009 A review of 3D vessel lumen segmentation techniques: models, features and extraction schemes *Med. Image Anal.* **13** 819–45
- Li H and Yezzi A 2007 Vessels as 4D curves: global minimal 4D paths to extract 3D tubular surfaces and centerlines *IEEE Trans. Med. Imaging* **26** 1213–23
- Lorensen H E and Cline W E 1987 Marching cubes: a high resolution 3D surface construction algorithm *Comput. Graph.* **21** 163–9
- Peker A, Uestuener E, Oezkavukcu E and Sancak T 2009 Performance analysis of 8-channel MDCT angiography in detection, localization and sizing of intracranial aneurysms identified on DSA *Neuroradiology* **15** 81–5
- Penney G, Weese J, Little J, Desmedt P, Hill D and Hawkes D 1998 A comparison of similarity measures for use in 2D–3D medical image registration *IEEE Trans. Med. Imaging* **17** 586–95
- Schuldhuis D, Spiegel M, Redel T, Polyanskaya M, Struffert T, Hornegger J and Doerfler A 2011 Classification-based summation of cerebral digital subtraction angiography series for image post-processing algorithms *Phys. Med. Biol.* **56** 1791–802
- Schuldhuis D, Spiegel M, Redel T, Polyanskaya M, Struffert T, Hornegger J and Doerfler A 2011 2D vessel segmentation using local adaptive contrast enhancement *Bildverarbeitung fuer die Medizin (Luebeck)* ed H Handels, J Ehrhardt, T Deserno, H Meinzer and T Tolxdorff (Berlin: Springer) pp 109–13
- Sherouse G W, Novins K and Chaney E L 1990 Computation of digitally reconstructed radiographs for use in radiotherapy treatment design *Int. J. Radiat. Oncol. Biol. Phys.* **18** 651–8
- Spiegel M, Redel T, Zhang Y, Struffert T, Hornegger J, Grossman R, Doerfler A and Karmonik C 2011 Tetrahedral versus polyhedral mesh size evaluation on flow velocity and wall shear stress for cerebral hemodynamic simulation *Comput. Methods Biomech. Biomed. Eng.* **14** 9–22
- Strobel N et al 2009 *Multislice CT* (Berlin: Springer)
- Tauber C, Batatia H and Ayache A 2009 Robust B-spline snakes for ultrasound image segmentation *J. Signal Process. Syst.* **54** 159–69
- Tek H, Ayvaci A and Comaniciu D 2005 Multi-scale vessel boundary detection *Computer Vision for Biomedical Image Applications (Lecture Notes in Computer Science)* vol 3765 (Berlin: Springer) pp 388–98

- Tyrrell J A, Tomaso E di, Fuja D, Tong R, Kozak K, Jain R K and Roysam B 2007 Robust 3D modeling of vasculature imagery using superellipsoids *IEEE Trans. Med. Imaging* **26** 223–37
- Wong W and Chung A 2007 Probabilistic vessel axis tracing and its application to vessel segmentation with stream surfaces and minimum cost path *Med. Image Anal.* **11** 567–87
- Yim P, Cebal J, Mullick R, Marcos H and Choyke P 2001 Vessel surface reconstruction with a tubular deformable model *IEEE Trans. Med. Imaging* **20** 1411–21
- Zellerhoff M, Scholz B, Ruehrnschopf E-P and Brunner T 2005 Low contrast 3D reconstruction from c-arm data *Proc. SPIE* **5745** 646–55